Chemosphere 262 (2021) 127671

Contents lists available at ScienceDirect

Chemosphere

journal homepage: www.elsevier.com/locate/chemosphere

Peroxidation and photo-peroxidation of pantoprazole in aqueous solution using silver molybdate as catalyst

Daniela G. Della Rocca [a], Henrique F.V. Victória [b], Camilla Daniela Moura-Nickel [a], Gidiane Scaratti [a], Klaus Krambrock [b], Agenor De Noni [a], Vítor J.P. Vilar [c], Humberto Jorge José [a], Regina F.P.M. Moreira [a, *]

[a] Laboratory of Energy and Environment (LEMA), Department of Chemical and Food Engineering, Federal University of Santa Catarina (UFSC), 88040-900, Florianópolis, SC, Brazil
[b] Department of Physics, Federal University of Minas Gerais (UFMG), 31270-901, Belo Horizonte, MG, Brazil
[c] Laboratory of Separation and Reaction Engineering - Laboratory of Catalysis and Materials (LSRE-LCM), Department of Chemical Engineering, Faculty of Engineering, University of Porto, Rua Do Dr. Roberto Frias, 4200-465, Porto, Portugal

HIGHLIGHTS

- Facile synthesis of Ag_2MoO_4 with both α and β-phases.
- α-Ag_2MoO_4 + β-Ag_2MoO_4 catalyst showed photocatalytic activity under visible light.
- Efficient oxidation of pantoprazole by catalytic peroxidation with Ag_2MoO_4.
- Mechanistic route for pantoprazole degradation via $^{\bullet}OH$ radicals is proposed.
- Almost complete toxicity removal of PAN and its by-products was observed in 2 h.

GRAPHICAL ABSTRACT

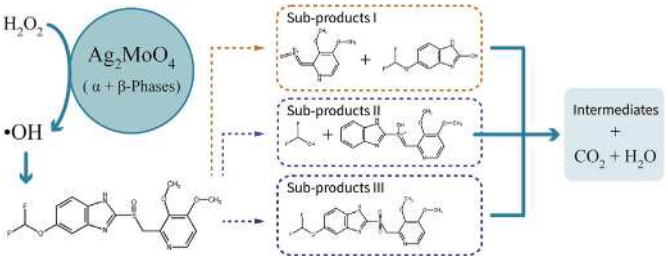

ARTICLE INFO

Article history:
Received 17 April 2020
Received in revised form
25 June 2020
Accepted 9 July 2020
Available online 11 August 2020

Handling Editor: Jun Huang

Keywords:
Ag_2MoO_4
Photocatalysis

ABSTRACT

In this study, silver molybdate was used as a catalyst in different oxidation processes to degrade pantoprazole (PAN) from aqueous suspension. The catalyst was synthesized using a controlled precipitation method and characterized by XRD, FTIR spectroscopy, BET analysis, Zeta potential, FEG-SEM/EDS, DRS and EPR. The α- and β-phases of Ag_2MoO_4 were identified as crystalline structure of the butterfly-shaped particles. The metastable α-phase could be completely converted into β-Ag_2MoO_4 by thermal treatment at 300 °C. The band gap energy of β-Ag_2MoO_4 (E_g = 3.25 eV) is slightly higher than for as-prepared catalyst (α-Ag_2MoO_4 + β-Ag_2MoO_4) (E_g = 3.09 eV), suggesting that as-prepared catalyst should be active under visible light. PAN is sensible to UV light irradiation, and the addition of H_2O_2 as electron acceptor enhanced the mineralization rate. In the catalytic UV-based reactions, high PAN oxidation efficiencies were obtained (>85%) but with low mineralization (32-64%). Catalytic peroxidation and photocatalytic peroxidation under visible light showed the highest PAN oxidation efficiency, leading to its

Abbreviations: $^{\bullet}OH$, Hydroxyl radical; Ag_2MoO_4, Silver molybdate; AOP, Advanced oxidation processes; DMPO, 5,5-dimethyl-pyrroline N-oxide; DRS, UV–Vis diffuse reflectance spectroscopy; DTA, Differential thermal analysis; E_{CB}, Conduction band energy; EDS, Energy dispersive spectrometer; E_g, Band gap energy; EPR, Electron paramagnetic resonance; E_{VB}, Valence band energy; FEG-SEM, Field emission gun scanning electron microscopy; FTIR, Fourier transform infrared spectroscopy; PAN, Pantoprazole; PBN, alpha-phenyl N-tertiary-butyl nitrone; PVP, Polyvinylpyrrolidone; ROS, Reactive oxygen species; S_{BET}, Brunauer-Emmett-Teller surface area; TEMP, 2,2,6,6-tetramethylpiperidine; TGA, Thermogravimetric analysis; TOC, Total organic carbon; UV, Ultraviolet; Vis, Visible; V_P, Total pore volume; XRD, X-ray diffraction.

* Corresponding author.
E-mail addresses: daniela.gier.della.rocca@grad.ufsc.br (D.G. Della Rocca), henrivic@hotmail.com (H.F.V. Victória), camilla.nickel@gmail.com (C.D. Moura-Nickel), gidiane@gmail.com (G. Scaratti), klaus@fisica.ufmg.br (K. Krambrock), agenor.junior@ufsc.br (A. De Noni), vilar@fe.up.pt (V.J.P. Vilar), humberto.jose@ufsc.br (H.J. José), regina.moreira@ufsc.br, regina.moreira@enq.ufsc.br (R.F.P.M. Moreira).

https://doi.org/10.1016/j.chemosphere.2020.127671

Advanced oxidation processes
Pharmaceuticals

almost complete mineralization (>95%), even under dark conditions (98% in 120 min). Several degradation byproducts were identified and three mechanistic routes of PAN decomposition were proposed. The identified byproducts are less toxic than the parent compound. EPR coupled with the spin trapping method identified •OH radicals as the main ROS species in both photocatalytic and catalytic peroxidation reactions. Ag_2MoO_4 showed to be a promising catalyst to promote the decomposition of hydrogen peroxide into ROS.[1]

1. Introduction

The demand on semiconductor particles for catalytic and photocatalytic processes has progressively increased due to their unique properties and versatile applications Recent advances in nanotechnology have stimulated extensive research investigating engineered nanocatalysts to produce active, stable and low cost catalyst to be applied in advanced oxidation processes (Hinojosa Guerra et al., 2019; Hosseini et al., 2018; Kumar et al., 2019; Penghui et al., 2017; Sharma et al., 2019).

Among these, silver molybdate (Ag_2MoO_4) has shown exceptional activity under visible light in the degradation of organic compounds (Cao et al., 2017; Huo et al., 2018; Moura et al., 2016). Two different crystalline phases (α-Ag_2MoO_4, with tetragonal structure and β-Ag_2MoO_4, with cubic structure) have been investigated, characterized and distinct electronic configurations have already been proposed (Arora et al., 2012; Beltrán et al., 2014; Donohue and Shand, 1947; Ng and Fan, 2015; Wyckoff, 1922). Moreover, according to Wang et al. (2017), the co-existence of α-Ag_2MoO_4 and β-Ag_2MoO_4 phases could contribute to a high photocatalytic activity under visible light. The reasons behind this achievement are not clear, since even the most studied photocatalyst, TiO_2, presents contradictory results about the effect of the co-existence of two different crystalline phases (anatase and rutile) on the photocatalytic activity (Apopei et al., 2014; Makal and Das, 2018; Wang et al., 2018).

Metastable phases of materials, such as α-Ag_2MoO_4, have been reported to exhibit physical and chemical properties which differ from those of their thermodynamically stable counterparts (Chen, 1997). However, because of the transformation of the metastable phase into its more stable phases, the synthesis of metastable α-Ag_2MoO_4 remains a challenge (Lu et al., 2001).

Different methods to synthetize α-Ag_2MoO_4 or β-Ag_2MoO_4 microcrystals with controlled shape and particle size have been proposed (Ng and Fan, 2015; Wang et al., 2017). Although the stable β-Ag_2MoO_4 is relatively easy to obtain at room temperature (Cunha et al., 2015), the synthesis of α-Ag_2MoO_4 frequently needs high hydrostatic pressure (Beltrán et al., 2014).

More recently, some reports have shown that it is possible to produce α- and β-Ag_2MoO_4 morphologies under mild conditions (Wang et al., 2017; Xu et al., 2015), for different applications considering their high electrical conductivity, photoluminescence, elevated energy storage performance, environmentally 'green' composition, antimicrobial, catalytic and photocatalytic properties (Bhattacharya and Ghosh, 2007; Cunha et al., 2015; Driscoll et al., 1994; Saha et al., 2019).

Considering the application in the photocatalysis field, Li et al. (2018) and Yang et al. (2017) reported that hydroxyl radicals (•OH) are produced on the illuminated Ag_2MoO_4 surface, showing an important contribution to the oxidation reactions. Due to these characteristics, Ag_2MoO_4 is not only promising for use in photocatalysis, but also in other advanced oxidation processes (AOP), particularly in peroxidation and photo-peroxidation. The band gap energy of the α-Ag_2MoO_4 phase is lower than that of β phase (1.26 and 3.01 eV vs 3.89 eV), enabling photocatalytic reactions under visible light (Ng and Fan, 2015).

Pantoprazole (PAN) (Fig. S1A) is one of the most commonly consumed drugs worldwide (Ortiz de García et al., 2013), and approximately 70–95% of the consumed PAN is excreted as inactive or pharmaceutically active metabolites in urine and feces (Kosma et al., 2016). PAN residues are present in domestic wastewaters, in concentrations of up to 0.18 μg L^{-1} (Barreiro et al., 2011; Gracia-Lor et al., 2012), and although PAN species (Fig. S1B) are unstable at acidic pH (Jungnickel, 2000), its removal and/or mineralization by wastewaters treatment plant has not been completely studied. PAN is well removed by adsorption onto iron-based nanoparticles (89% removal in 30 min) (Ali et al., 2016), but the mineralization efficiency through AOPs (e.g. heterogeneous Fenton-like processes using Fe_3O_4/CeO_2) is rather low (Gan et al., 2017).

In this context, the main goal of this study is to develop a fast method to synthesize highly efficient catalysts based on Ag_2MoO_4 for application in AOPs to degrade PAN.

2. Material and methods

2.1. Chemicals and materials

Silver acetate (98% purity), and polyvinylpyrrolidone (PVP, Mw ≈ 40,000 g mol^{-1}) were obtained from NEON. Ammonium molybdate and H_2O_2 (30%, analytical purity) were obtained from Vetec. TiO_2—P25 was supplied by Evonik-Degussa (particle size < 50 nm, 80% anatase and 20% rutile) (Vieira et al., 2018). The pharmaceutical PAN (99.5% purity, Pharmanostra (Brazil). and all reagents were used without further purification.

2.2. Catalyst synthesis

The Ag_2MoO_4 catalyst was synthesized at room temperature by a modified controlled precipitation method (Wang et al., 2017). First, 1 mmol of silver acetate was dissolved in 50 mL of deionized water, then 7.4 mmol of PVP was added as stabilizing agent to avoid particle agglomeration. Subsequently, 2.5 mL of ammonium molybdate (0.0285 M) were added drop by drop to form a white solid. After stirring for 30 min, the solids were filtered through PVDF membranes (Durapore, 0.22 μm), dried at 60 °C overnight, and micronized by maceration. Fig. S2 shows a schematic flowchart of this methodology. A sample of the as-prepared catalyst was calcined in an oven at 300 °C under air atmosphere, for 3 h.

2.3. Characterization

X-ray diffraction (XRD) data were recorded using a Rigaku Miniflex II diffractometer with CuK_α radiation (λ = 1.5418 Å), in the range between 10 and 70° (0.05°·s^{-1} scan speed), operating at 30 kV and 15 mA. Thermogravimetric analysis (TGA) and differential thermal analysis (DTA) were conducted on a Shimazdu

thermogravimeter (model DTG60/60H) under inert atmosphere (N_2, 99.996% purity) at a heating rate of 10 °C min^{-1} from ambient temperature to 350 °C. Field emission gun scanning electron microscopy (FEG-SEM) was carried out using a JEOL JSM-6701 F microscope, which was coupled with an energy dispersive spectrometer (EDS). The Brunauer-Emmett-Teller surface area (S_{BET}) and pore diameter distribution were determined by nitrogen (N_2) adsorption-desorption experiments using an adsorptometer (Autosorb 1C analyzer, Quantachrome, USA). The UV–Vis diffuse reflectance spectroscopy (DRS) and Fourier transform infrared (FTIR) spectroscopy were investigated using a PerkinElmer UV/Vis/NIR Lambda 750 spectrometer and an infrared spectrophotometer Agilent Technologies, Cary 600 Series, respectively.

2.4. Reactive oxygen species (ROS) formation

Formation of ROS was studied by electron paramagnetic resonance (EPR) allied with the spin trapping method on commercial X-band (9.4 GHz) Miniscope 400 spectrometer (Magnettech, Germany). ROS formation was investigated under UV light and for peroxidation reactions using three different spin traps: DMPO (5,5-dimethyl-pyrroline N-oxide), PBN (alpha-phenyl N-tertiary-butyl nitrone) and TEMP (2,2,6,6-tetramethylpiperidine). For the study of UV reactions, aqueous solutions (2 mL) containing the spin traps DMPO (0.3 M) or TEMP (1 M) with 10 mg of Ag_2MoO_4 catalyst were illuminated with a white LED lamp (16 mW cm^{-2}) calibrated by a Coherent Lasermate/D power meter. After different time intervals, 50 μL aliquots were filled into glass capillaries, sealed and analyzed by EPR inside a quartz tube (Wilmad Labglass). For the peroxidation studies, H_2O_2 (100 μL, 5%) was added to the same spin trap solutions, as previously. After different time intervals, 50 μL aliquots were analyzed. Experimental parameters used for EPR were: microwave power 10 mW, 100 kHz field modulation amplitude 0.2 mT, and central field 337 mT, and scan time 60 s. For the experiments with spin trap PBN (0.2 M) the aqueous solution was substituted by a mix of water and ethanol (1:1).

2.5. PAN degradation and mineralization using catalytic peroxidation under dark or light (UV/Vis) irradiation

All experiments were performed in a batch system, at 20 °C, using a continuously stirred 1 L-jacketed annular reactor (~600 rpm, Dist, model DI-03, Brazil), previously described by Vieira et al. (2018). A volume of 750 mL of PAN solution (0.2 g L^{-1}, $pH_0 = 9.2$) and catalyst (0.5 g L^{-1}) were placed in the reactor. To better evaluate the catalyst activity on the PAN degradation and mineralization, it was used a PAN concentration higher than the environmentally levels.

The peroxidation of PAN was studied using 0.5 g L^{-1} of H_2O_2. As-prepared Ag_2MoO_4 was applied, since prior photocatalytic experiments (paper in preparation) revealed that the calcined sample is less active than the as-prepared Ag_2MoO_4. Experiments were conducted under dark conditions or combined with a light source (UVA/Vis lamp, 200–800 nm, maximum peak at 368 nm, 41 W, Osram; or a LED visible lamp 400–800 nm, 2 W, Brilia), according to Vieira et al. (2018).

At regular time intervals, 15 mL aliquots were collected from the reactor, filtered and analyzed. PAN concentration was monitored in its maximum absorption wavelength, 289 nm (HACH, model DR5000). The mineralization was determined based on total organic carbon (TOC) measurements (TOC-TN VCPH, Shimadzu, Japan). Intermediates were identified by MS/MS (50–3000 m/z) in micrOTOF-Q II (Bruker) equipment, ESI source, positive ion polarity, capillarity 4500 V. The dry gas heater was maintained at 200 °C and the dry gas flux was 4.0 L min^{-1}. Ultrapure water was applied as solvent media. The H_2O_2 concentration decay was measured using the metavanadate method (Nogueira et al., 2005).

2.6. Acute toxicity test

The acute toxicity tests were performed for peroxidation kinetics with *Aliivibro fischeri* bacteria (BIOLUX, Brazil) in Microtox® equipment, by ISO 11348–3 procedure (Standard, 2007). The lyophilized bacteria were rehydrated with reactivation buffer (BIOLUX).

3. Results and discussion

3.1. Characterization of Ag_2MoO_4

The morphology of the Ag_2MoO_4 catalyst was investigated using FEG-SEM images. Fig. S3 shows agglomerates of smooth particles that have irregular forms and sizes (1–5 μm). The as-prepared Ag_2MoO_4 showed the presence of some butterfly-like structures, consisting of four united petals. When the structures were analyzed in detail it was observed that they were mostly comprised of either tiny butterfly-like shapes or had the appearance of petals parted from one another. The elemental composition of the solid was analyzed by EDS (Table 1), and proved the purity of the catalysts by the presence of oxygen, molybdenum and silver, with an Ag:Mo molar ratio near to the stoichiometric value (2:1).

The XRD results for the as-prepared sample are reported in Fig. S4A. The high crystallinity of the sample was evidenced by the presence of intense and sharp peaks. The two major peaks ($2\theta = 29.86°$ and 32.69°) correspond to the reflections (004) and (310) of tetragonal α-Ag_2MoO_4 (JCPDS 21–1340). The third largest peak ($2\theta = 31.94°$) is associated with the crystal plane (311) of cubic β-Ag_2MoO_4 (JCPDS 08–0473). In the as-prepared sample the estimated percentage of α-phase is 61% and 18% of β-phase and, the remaining amount was considered an amorphous phase (21%). After calcination at 300 °C, a complete phase transformation (α-Ag_2MoO_4 → β-Ag_2MoO_4) occurred, and only β-Ag_2MoO_4 (JCPDS 08–0473) is found (Fig. S4A); the proportion estimated is 82% and 18% for β-Ag_2MoO_4 and amorphous phase, respectively. Crystallite sizes obtained for the α and β phases of the as-prepared catalyst was slightly higher than the calcined sample (β-Ag_2MoO_4) (Table 1).

The high concentration of PVP used in the synthesis contributed

Table 1
Summary of the catalysts characteristics.

Characteristic	As-prepared catalyst	Calcined catalyst
Composition	α-Ag_2MoO_4 + β-Ag_2MoO_4	β-Ag_2MoO_4
Crystallite size (nm)	46 ± 0.3 (α); 41 ± 0.3 (β)	39 ± 0.3 (β)
DTA peaks	272 °C (exo); 318 °C (exo)	a
FTIR peaks (cm^{-1})	824; 1647; 3442	823; 1643; 3404
S_{BET} ($m^2 \cdot g^{-1}$)	1.9	a
Total pore volume V_P ($cm^3 \cdot g^{-1}$)	0.003	a
Average pore size (nm)	5.9	a
Isoelectric point	3.08	a
EDS element composition (wt %)	Ag (55.3); Mo (26.3); O (18.4)	a
Band gap energy, E_g (eV)	3.09	3.25
Conduction band energy, E_{CB} (eV)	−0.12	−0.21
Valence band energy, E_{VB} (eV)	2.96	3.05

a. Experiment not performed".

to the formation of two phases of Ag_2MoO_4 (Ng and Fan, 2015), since the groups of PVP, particularly C=O, can interact with metal ions and form a complex (Bönnemann and Nagabhushana, 2008; Jiang et al., 2004). The presence of PVP in the synthesis changes not only the particle size of the dispersed particles but also the accessibility at the surface (Teranishi and Miyake, 1998).

Fig. S4B shows the TGA and DTA curves of the as-prepared Ag_2MoO_4. The TGA curve shows no appreciable weight loss in the temperature range of 40–350 °C. Two exothermic peaks were detected in the DTA. The first, at 272 °C, is attributed to the phase change from α → β-Ag_2MoO_4 (Beltrán et al., 2014). The peak at 318 °C can be ascribed to the transformation of β-Ag_2MoO_4 into another new phase (uncharacterized up to this time), indicating a possible thermal instability of the β-phase. According to Moura et al. (2016), this phase was also identified in the Raman and XRD measurements, described as a phase transition: cubic → unknown phase.

The FTIR spectra (Fig. S5) of the catalysts exhibit the characteristic peaks at around 824 cm^{-1}, corresponding to the antisymmetric stretching vibrations of O–Mo–O. Peaks around 1640 cm^{-1} and 3400 cm^{-1} were ascribed to the bending vibration of absorbed water and surface hydroxyl *O*–H stretching, respectively.

The N_2 adsorption-desorption isotherms at 77 K of the as-prepared Ag_2MoO_4 is classified as type II (Thommes et al., 2015), showing a discrete H3-hysteresis, typical of plate-like particles (Fig. S6). The S_{BET} value (Table 1) is similar to those previously reported for α- and β-Ag_2MoO_4 phases (Huo et al., 2018; Li et al., 2018), indicating that the coexistence of the two phases of Ag_2MoO_4 should not lead to differences in the textural characteristics.

The zeta potential data of the as-synthesized Ag_2MoO_4 sample (Fig. S7) shows that the particle is negatively charged in all the measured pHs between ~3 and 10, i.e., its surface is negatively charged for a large pH range.

The UV–Vis reflectance spectra for the as-prepared and calcined Ag_2MoO_4 are shown in Figs. S8A and a maximum peak is observed at ~320 nm. The absorption edge of the catalyst at 465 nm indicates its potential application in the visible spectral region for catalytic purposes. The direct calculated band gaps for as-prepared and calcined samples (Fig. S8B and Table 1) are lower than those reported by other authors for materials with different particle morphology (Cao et al., 2017; Oliveira et al., 2017; Xu et al., 2015). The decrease in E_g can be attributed to structural defects in the medium range and local bond distortions, which yield localized electronic levels within the forbidden band gap (Sousa et al., 2018). This is expected due to the coexistence of both α-Ag_2MoO_4 and β-Ag_2MoO_4 phases (Ng and Fan, 2015).

The E_{CB} and E_{VB} values (Table 1) were calculated according to Equations 3 and 4 (Supplementary material). For a given photocatalytic redox reaction, the E_{CB} value should be more negative than the electron acceptor redox potential, while the E_{VB} should be more positive than the oxidation potential of the chemical oxidizable compounds. So, it could be expected that different ROS are in the presence of different electron acceptors, considering the different Ag_2MoO_4 crystalline phases.

To study the ROS, EPR spin trapping measurements were performed. Using DMPO, the most intense EPR spectrum occurred for an illumination time of 16 min and is shown in Fig. 1A. The EPR spectrum consists of two contributions of DMPO spin adducts: (i) DMPO* (c), which is a spin adduct associated with DMPO degradation resulting from protonation of the spin trap molecule and (ii) DMPO/*OH (d), which is formed by capture of hydroxyl radicals. The spin Hamiltonian parameters are a_N = 14.6 G and $a_N = a_{H(\beta)}$ = 14.9 G for DMPO* and DMPO/*OH, respectively (Bilski et al., 1996; Hensley et al., 1995; Zhao et al., 2001). The sum of both calculated EPR spectra is shown in Fig. 1 (B) and it represents well the measured spectrum.

To test the catalytic activity of Ag_2MoO_4 with H_2O_2 in the dark, another spin trapping experiment was done using the same DMPO spin trap. The formation of spin adducts by the addition of H_2O_2 occurred very fast, more specifically, the highest DMPO spin adduct concentration was detected for the first aliquot (~after 2 min of reaction). The corresponding EPR spectrum is shown in Fig. 1B. The same spin adducts, i.e. DMPO* and DMPO/*OH, were identified as it was the case after UV light illumination (Fig. 1A). Due to the low stability of DMPO adducts a kinetic study could not be done. To study the kinetics of hydroxyl radical formation after the addition of H_2O_2, DMPO was replaced by PBN spin trap. Figure 2A shows a typical measured EPR spectrum obtained after 10 min of interaction between Ag_2MoO_4 catalyst, H_2O_2 and PBN in ethanol/water solution.

The EPR spectrum of the PBN adducts shows the superposition of two distinct spin adducts. In cases where the concentration of hydroxyl radicals is small compared with the amount of ethanol, the reaction of capture of this free radical with PBN becomes suppressed. Therefore, a radical species captured by PBN is given by the product of the interaction of hydroxyl radical with ethanol

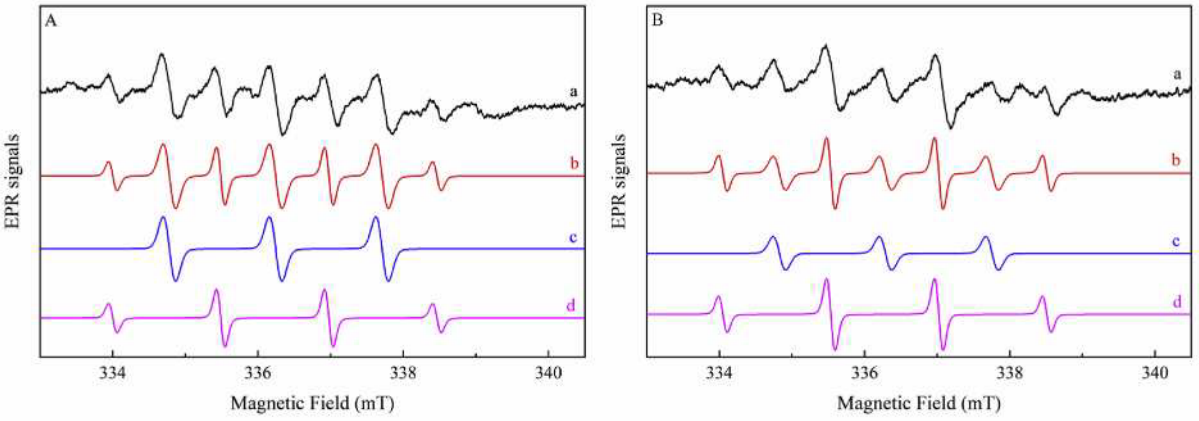

Fig. 1. EPR spectra of DMPO adducts (a) obtained of aqueous solution containing DMPO and Ag_2MoO_4: (A) after 16 min illumination by white light and (B) immediately after addition of H_2O_2. The lines correspond to calculation of EPR spectra using the Easyspin® software (Stoll and Schweiger, 2006) for two different DMPO spin adducts: protonated DMPO* adduct (c) and DMPO/*OH adduct (d) and sum of both spectra (b).

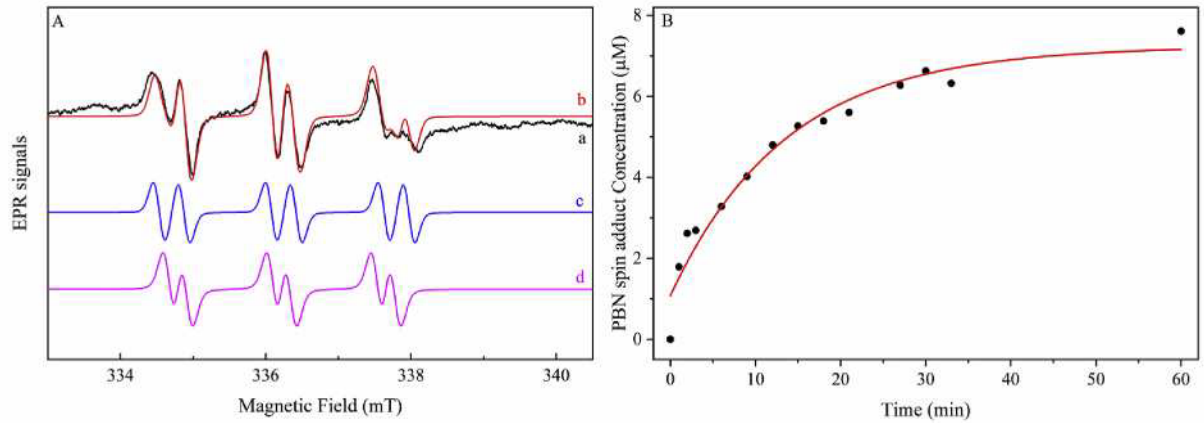

Fig. 2. (A) EPR spectrum of PBN adducts (a) obtained after addition of H_2O_2 to ethanol/water solution in the presence of Ag_2MoO_4 catalyst. Calculated EPR spectra using the Easyspin® software are shown in (c) and (d), and their sum in (b). (B) Kinetic evolution of the absolute PBN spin adduct concentration as a function of reaction time.

molecule leading to spin adducts of ethoxy and/or α-hydroxyethyl radicals (Rosen et al., 1999). Therefore, the resulting EPR spectrum throughout the reaction is given by the competition between capture/generation of these two spin adducts with spin Hamiltonian parameters $a_N = 14.4$ G and $a_{H(\beta)} = 2.4$ G (ethoxy radicals) and with $a_N = 15.5$ G and $a_{H(\beta)} = 3.4$ G (α-hydroxyethyl radicals) (Ledwith et al., 1973; Saprin and Piette, 1977). Fig. 2B presents the kinetic evolution of the PBN adducts as a function of time after addition of H_2O_2. The absolute spin adduct concentrations were obtained from the double integration of the EPR spectra and compared to a known TEMPOL solution in water (10 mM). In addition, spin trapping experiments using TEMP spin trap instead of DMPO did not reveal spin adduct formation, as expected, since TEMP is a specific trap for oxygen singlet, $^1O_2$.

From the spin trapping experiments with both PBN and DMPO spin traps it was concluded that the dominant reactive oxygen species in the catalytic processes with Ag_2MoO_4 catalyst are due to the formation of hydroxyl radicals. For the peroxidation in dark, the probable mechanism of formation of the hydroxyl radical will be given by a typical Fenton reaction, in which the oxidation of Ag_2MoO_4 occurs and the formation of the ion and hydroxyl radical pair (Fig. S9). Meanwhile, reactions with white light form electron/hole (e^-/h^+) pairs which then transfer charges to molecules of the solvent leading to the generation of hydroxyl radicals.

3.2. PAN removal using Ag_2MoO_4

PAN is fairly resistant to degradation under visible light and by H_2O_2 oxidation, while it adsorbs in appreciable amounts onto the as-prepared Ag_2MoO_4 (Fig. 3A) (non-calcined sample). When H_2O_2 was not added to the reaction medium, a significant adsorption of PAN on Ag_2MoO_4 was observed, which is not due to the electrostatic interactions at barely basic pH (8–9) (Fig. S10), since the negatively surface of the catalyst (Fig. S7) is not able to electrostatically interact with the neutral PAN species.

On the other hand, the photolysis of PAN with UV light leads to a considerable decay in the absorbance at 289 nm, without mineralization (Raffin et al., 2008). Thus, it is assumed that sub-products of PAN are formed during its photolysis, which could be more resistant or less reactive in the presence of the catalyst, since low TOC removal was observed. Besides, probably different mechanisms occur when PAN is degraded under UV light or others light sources, as reported by Raha and Ahmaruzzaman (2020).

It is important to emphasize the high efficiency of the as-prepared Fenton-like process, since the PAN degradation and mineralization achieved 98% and 93%, respectively in 120 min. These results are more relevant than those reported previously using Fe_3O_4/CeO_2 or $ZnO/Fe_3O_4/g\text{-}C_3N_4$ in catalytic peroxidation processes (Gan et al., 2017; Raha and Ahmaruzzaman, 2020).

Furthermore, studies were also performed without H_2O_2 addition in the presence of UV or visible light (Ag_2MoO_4 + UV and Ag_2MoO_4 + Vis) and the PAN mineralization efficiencies after 120 min were, respectively, 64% and 56%, i.e., at least 29% lower than that measured in the presence of H_2O_2. These results indicated that a more efficient electron acceptor, such as hydrogen peroxide, is required to achieve high mineralization rate.

Figure 3A shows that the highest TOC removal was obtained in the catalytic peroxidation. The decrease in the pH (Fig. S10) caused by PAN degradation using UV-light is associated to a fast PAN degradation (Fig. S10), but with low mineralization efficiency, indicating that different types of ROS are formed in the light-enhanced processes in relation to catalytic peroxidation.

Fig. 3B also evidences the fast mineralization of PAN by as-prepared Ag_2MoO_4 peroxidation and photo-peroxidation. In 5 min, high TOC removal levels were observed (>48%). Furthermore, the kinetics reinforces that UV light lead to more recalcitrant products, since approximately only 23% of PAN fully oxidizes into CO_2, showing that the generated intermediates slow down the reaction.

Under UV-light TiO_2–P25 is somewhat better than Ag_2MoO_4, while the photocatalytic activity of TiO_2–P25 under visible light is lower than Ag_2MoO_4. This result is due to the low absorptivity (high reflectance) of TiO_2–P25 on the visible region (Valeeva et al., 2018), while the as-prepared Ag_2MoO_4 presents higher absorptivity in the visible spectra (Fig. S8).

Peroxidation with as-prepared Ag_2MoO_4 under dark presents a mineralization pseudo-first-order kinetic constant (Fig. 3C) two-times higher than Vis + Ag_2MoO_4 + H_2O_2 and, approximately, 80 times higher than the best TiO_2–P25 peroxidation reaction (UV + TiO_2–P25 + H_2O_2). The Abs/Abs_0 (289 nm) of the performed oxidation reactions is shown in Fig. S11.

For H_2O_2 oxidation systems, PAN mineralization is associated with a consumption of oxidant (Fig. S12). A pseudo-first-order kinetic model describes well the H_2O_2 decomposition for peroxidation reactions, and Ag_2MoO_4 + H_2O_2 system showed the highest kinetic constant value (Table 2), reinforcing the elevated oxidizing potential of this process. The H_2O_2 decomposition constant is about one third of the mineralization constant, possibly being the limiting reaction. The as-prepared Ag_2MoO_4 peroxidation reactions, under dark and under visible light, had the best cost-benefit mole H_2O_2

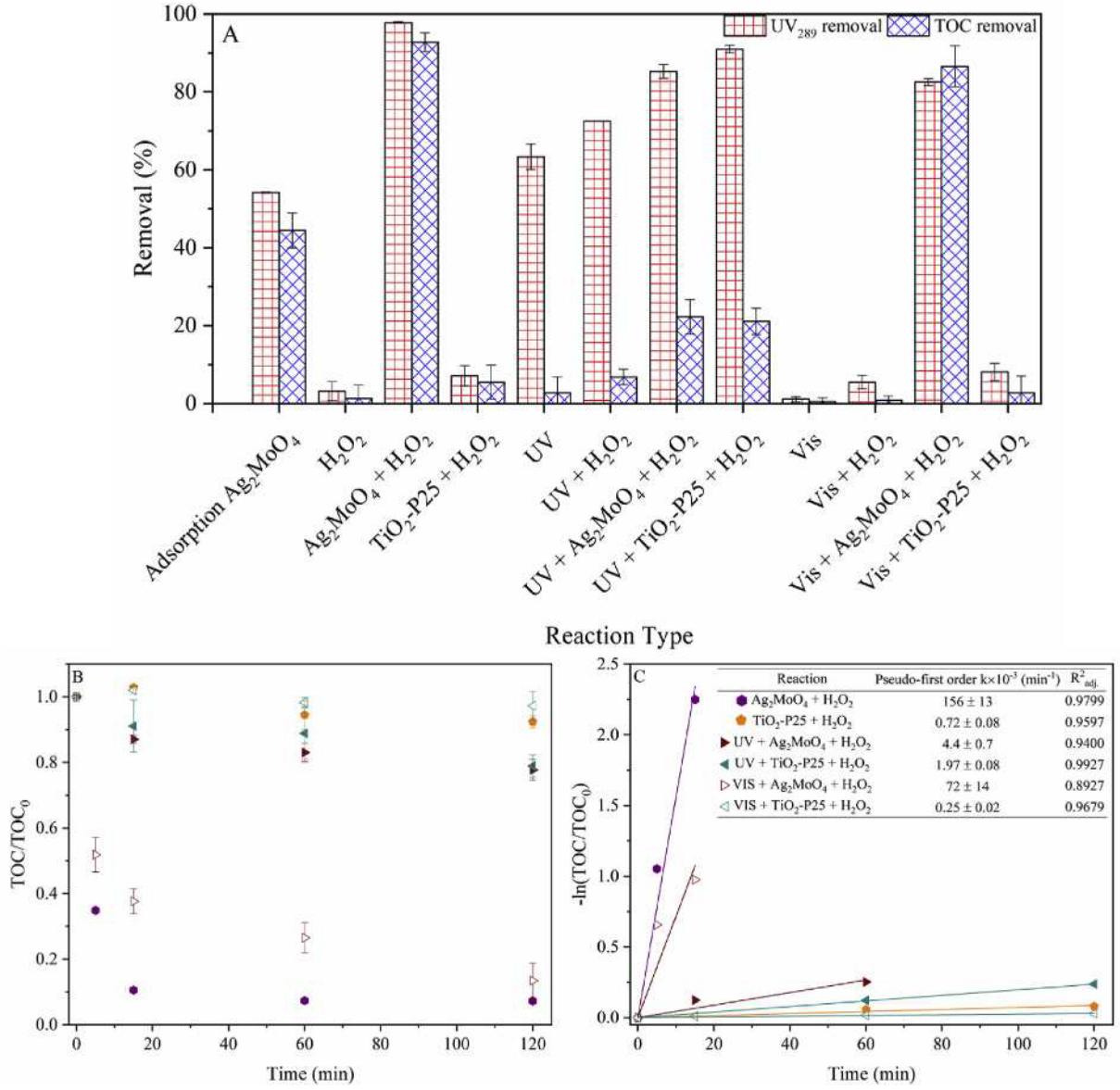

Fig. 3. (A) Degradation and mineralization of PAN after 2 h of treatment under similar experimental conditions ($pH_0 = 9.15$; $[PAN]_0 = 0.2$ g L^{-1}; $[TOC]_0 = 0.1$ g L^{-1}; solid dosage (when applied) = 0.5 g L^{-1}); (B) PAN mineralization kinetics and (C) pseudo-first order model applied for peroxidation reactions ($pH_0 = 9.15$; $[PAN]_0 = 200$ mg/L; $[TOC]_0 = 100$ mg/L; solid dosage (when applied) = 500 mg/L): ● $Ag_2MoO_4 + H_2O_2$, ⬟ - TiO_2–P25 + H_2O_2, ▶ - UV + $Ag_2MoO_4 + H_2O_2$, ◀ - UV + TiO_2–P25 + H_2O_2, ▷ - Vis + $Ag_2MoO_4 + H_2O_2$ and ◁ Vis + TiO_2–P25 + H_2O_2.

Table 2
Pseudo-first-order kinetics constant for H_2O_2 decomposition applying different oxidation systems ($pH_0 = 9.15$; solid dosage = 500 mg/L).

AOP applied for PAN degradation	Pseudo-first-order kinetics constant for H_2O_2 decomposition		mole H2O2 consumed mole PAN removed
	$k \times 10^{-2}$ (min^{-1})	$R^2_{adj.}$	
H_2O_2	~0	–	–
$Ag_2MoO_4 + H_2O_2$	5.0 ± 0.5	0.9547	31 ± 9
TiO_2–P25 + H_2O_2	~0	–	–
UV + H_2O_2	0.20 ± 0.03	0.8974	84 ± 6
Vis + H_2O_2	~0	–	–
UV + $Ag_2MoO_4 + H_2O_2$	0.90 ± 0.10	0.9041	58 ± 7
UV + TiO_2–P25 + H_2O_2	0.50 ± 0.04	0.9682	88 ± 26
Vis + $Ag_2MoO_4 + H_2O_2$	0.80 ± 0.09	0.9474	21 ± 1
Vis + TiO_2–P25 + H_2O_2	~0	–	–

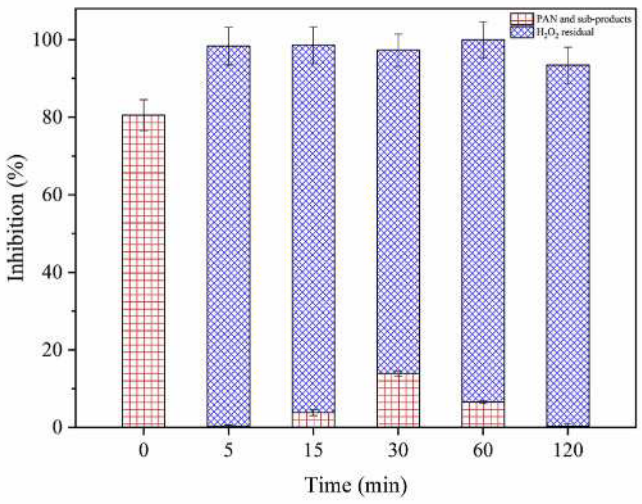

Fig. 4. Inhibition of *Aliivibro fischeri* luminescence intensity during specific reaction times using Ag_2MoO_4 peroxidation under dark.

consumed/mole of PAN removed ratio (Table 2).

The toxicity results of PAN and generated oxidation intermediates were obtained by subtracting the measured total inhibition from the value obtained from an aqueous solution containing the same residual hydrogen peroxide concentration than that present after reactions (Fig. S14). It is worth to mention that H_2O_2 was not removed from the aqueous solution prior to toxicity assessment, so the synergetic effect of PAN, its intermediates and residual H_2O_2 was estimated, as proposed by Márquez et al. (2018). Moreover, by measuring of H_2O_2 residual concentration and its toxicity, it was possible to estimate the PAN and its intermediate compounds by difference of the total toxicity (Fig. 4).

Addition of H_2O_2 causes a toxicity increase in first minutes of reaction but it also enhances the detoxification process leading to almost 100% reduction of toxicity of PAN and its by-products after 2 h of treatment. Besides, although the concentration of Ag and Mo ions have not been measured, it is reasonable to suppose that their concentration is low and could not contribute to the residual toxicity.

These results indicate that further studies should be performed to optimize the H_2O_2 concentration and a lower dosage could be used in the treatment. Since, complete mineralization is not always necessary and catalytic peroxidation, in the case of PAN, could be used in combination with other techniques as microbial action (biodegradation).

3.3. Proposed mechanistic routes for PAN oxidation

Eleven possible intermediates were identified for the PAN oxidation using as-prepared Ag_2MoO_4 peroxidation process (sample taken at 120 min of reaction), and their characteristics are presented in Table S1. The obtained MS/MS data is disposed in Supplementary Material (Fig. S13).

Three mechanisms pathways (Fig. 5) could be suggested according to the intermediates identified. First, both protonated forms (Na^+ or H^+) of PAN were detected, D0 ($m/z = 405$) and D1 ($m/z = 383$). Subsequently, as expected, PAN's oxidation through heterogeneous peroxidation showed high complexity of consecutive

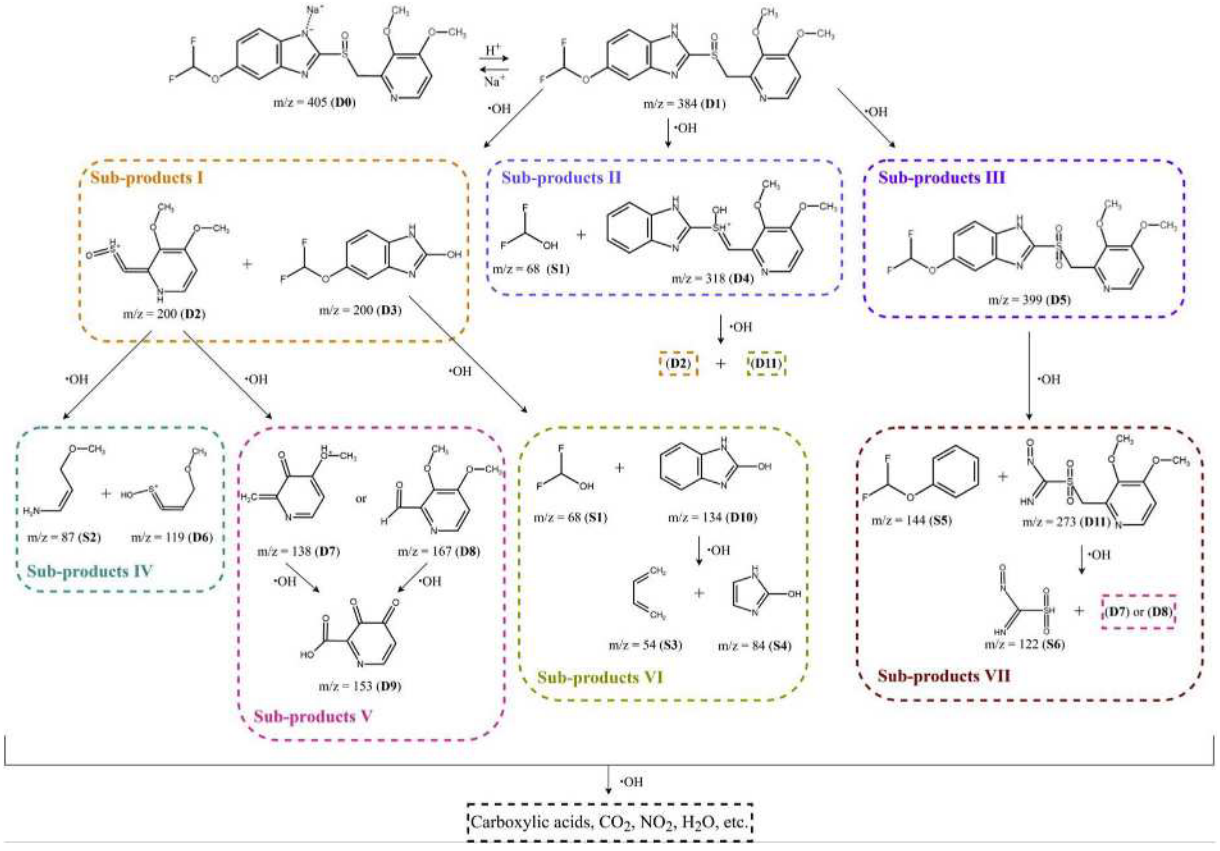

Fig. 5. Proposed mechanism routes for PAN oxidation.

and parallel reactions. In the first pathway (sub-products I), PAN's sulfur bond was broken, forming D2 (m/z = 200) and D3 (m/z = 200), being the imidazole group hydroxylated, forming an alcohol. For the other pathways (sub-products II and III) it can be noted that the sulfur was oxidized, forming distinct intermediates, −D4 (m/z = 318), S1 (m/z = 68) and D5 (m/z = 399) − this is due to its lone electron pair which has tendency of oxidizing, forming sulfenic acid and sulfone group, respectively. Following, these intermediates are further oxidized. For D2, it may follow two routes (sub-products IV and V): cleavage of the pyridine ring, generating D6 (m/z = 119) and S2 (m/z = 87), or both desulfonation and oxidation of the molecule, leading to D7 (m/z = 138) or D8 (m/z = 167), which are once again oxidized forming D9 (m/z = 153). Moreover, the ether bond of D3 is attacked by a hydroxyl radical, breaking and transforming it into S1 and D10 (m/z = 134) (sub-products VI). Also, the benzene ring of D10 then ruptures into S3 (m/z = 54) and S4 (m/z = 84). Likewise, D4 intermediate breaks into D2 and D10, following the already described reactions.

Yet, the last degradation mechanism (sub-products VII) produced different species from the previous pathways discussed above. In this case, the imidazole group of D5 cleavages, generating both D11 (m/z = 273) and S5 (m/z = 144). After, D11 is attacked by $^{\bullet}OH$, separating the sulfone group, producing S6 (m/z = 122) and, after another oxidation reaction, generate D8 or D9, which proceed to other reactions already described.

Subsequently, these cited smaller molecules can be successively degraded, forming simpler carboxylic acids and even be totally mineralized to products as CO_2, NO_3^- and H_2O.

4. Conclusions

In this study, a novel mixed catalyst with both α and β phases of Ag_2MoO_4 was successfully synthesized using a simple controlled precipitation method and applied in peroxidation and photo-peroxidation reactions (Ag_2MoO_4+H_2O_2, Ag_2MoO_4+H_2O_2 + UV, Ag_2MoO_4+H_2O_2 +Vis) of a micropollutant, pantoprazole (PAN). The best catalyst performance was obtained for peroxidation and Vis photo-peroxidation reactions, leading to an almost complete PAN mineralization. Hydroxyl radicals were identified as the dominant ROS formed during the catalytic reactions, either in the presence of light or hydrogen peroxide. For the peroxidation in dark, the probable mechanism of formation of the hydroxyl radical could be described as a typical Fenton reaction, while under light irradiation, the electron/hole (e^-/h+) pairs are formed and then transferred to molecules of the H_2O_2, leading to the generation of hydroxyl radicals.

The UV-based reactions showed high degradation levels, but PAN's mineralization was very inefficient, indicating that this compound is very sensitive to light and resistant by-products are formed. A complex mechanism was proposed for the first time considering the sub-products formed by catalytic peroxidation using silver molybdate. Eleven possible intermediates were identified by the PAN oxidation using as-prepared Ag_2MoO_4. In parallel, the acute toxicity decreased due to the PAN oxidation indicating that less toxic intermediate products were formed. The residual hydrogen peroxide after reactions contributed to the high acute toxicity, suggesting that further studies should be performed to optimize the H_2O_2 concentration required to achieve high PAN degradation and low residual toxicity.

Overall, it can be concluded that this novel application of α-Ag_2MoO_4/β-Ag_2MoO_4 as a catalyst for peroxide oxidation reactions provides not only an efficient process but also represents a promising approach, since it easily transformed PAN into more easily biodegradable products.

Credit author statement

Daniela G. Della Rocca: Conceptualization, Methodology, Investigation, Writing - original draft: Writing - review & editing; Henrique F.V. Victória: Investigation; Camilla Daniela Moura-Nickel: Visualization; Gidiane Scaratti: Conceptualization, Methodology and Writing - Review & Editing; Klaus Krambrock: Conceptualization, Formal analysis, Writing - review & editing; Agenor de Noni Jr: Formal analysis; Vítor J.P. Vilar: Conceptualization and Writing - Review & Editing; Humberto Jorge José; : Resources and Validation; Regina F. P. M Moreira: Conceptualization, Writing - review & editing, Supervision, Project administration and Funding acquisition

Declaration of competing interest

The authors declare that they have no known competing financial interests or personal relationships that could have appeared to influence the work reported in this paper.

Acknowledgements

The authors would like to acknowledge the Coordination of Improvement of Higher Education Personnel (CAPES - Brazil) [Grant code 001; and CAPES /PrInt Project number 88887.310560/2018−00] and Brazilian Council for Scientific and Technological Development (CNPq - Brazil) [Grant 405892/2013 6] for financial support, as well as LCME (Central Laboratory of Electronic Microscopy), and CEBIME (Multiplier Mass Spectrometry Laboratory). This work was also financially supported by Base Funding - UIDB/50020/2020 of the Associate Laboratory LSRE-LCM - funded by national funds through FCT / MCTES (PIDDAC). Vítor J.P. Vilar acknowledge the FCT Individual Call to Scientific Employment Stimulus 2017 (CEECIND/01317/2017).

Appendix A. Supplementary data

Supplementary data to this article can be found online at https://doi.org/10.1016/j.chemosphere.2020.127671.

References

Ali, I., Al-Othman, Z.A., Alharbi, O.M.L., 2016. Uptake of pantoprazole drug residue from water using novel synthesized composite iron nano adsorbent. J. Mol. Liq. 218, 465−472. https://doi.org/10.1016/j.molliq.2016.02.088.

Apopei, P., Catrinescu, C., Teodosiu, C., Royer, S., 2014. Mixed-phase TiO_2 photocatalysts: crystalline phase isolation and reconstruction, characterization and photocatalytic activity in the oxidation of 4-chlorophenol from aqueous effluents. Appl. Catal. B Environ. 160−161, 374−382. https://doi.org/10.1016/j.apcatb.2014.05.030.

Arora, A.K., Nithya, R., Misra, S., Yagi, T., 2012. Behavior of silver molybdate at high-pressure. J. Solid State Chem. 196, 391−397. https://doi.org/10.1016/j.jssc.2012.07.003.

Barreiro, J.C., Vanzolini, K.L., Cass, Q.B., 2011. Direct injection of native aqueous matrices by achiral-chiral chromatography ion trap mass spectrometry for simultaneous quantification of pantoprazole and lansoprazole enantiomers fractions. J. Chromatogr. A 1218, 2865−2870. https://doi.org/10.1016/j.chroma.2011.02.064.

Beltrán, A., Gracia, L., Longo, E., Andrés, J., 2014. First-principles study of pressure-induced phase transitions and electronic properties of Ag_2MoO_4. J. Phys. Chem. C 118, 3724−3732. https://doi.org/10.1021/jp4118024.

Bhattacharya, S., Ghosh, A., 2007. Silver molybdate nanoparticles, nanowires, and nanorods embedded in glass nanocomposites. Phys. Rev. B Condens. Matter 75, 2−5. https://doi.org/10.1103/PhysRevB.75.092103.

Bilski, P., Reszka, K., Bilska, M., Chignell, C.F., 1996. Oxidation of the spin trap 5,5-dimethyl-1-pyrroline N-oxide by singlet oxygen in aqueous solution. J. Am. Chem. Soc. 118, 1330−1338. https://doi.org/10.1021/ja952140s.

Bönnemann, H., Nagabhushana, K.S., 2008. Metal Nanoclusters in Catalysis and Materials Science. Elsevier. https://doi.org/10.1016/B978-0-444-53057-8.X5001-6.

Cao, W., An, Y., Chen, L., Qi, Z., 2017. Visible-light-driven Ag_2MoO_4/Ag_3PO_4 composites with enhanced photocatalytic activity. J. Alloys Compd. 701, 350−357.

https://doi.org/10.1016/j.jallcom.2016.12.436.
Chen, C., 1997. Size dependence of structural metastability in semiconductor nanocrystals. Science 276, 398–401. https://doi.org/10.1126/science.276.5311.398, 80.
Cunha, F.S., Sczancoski, J.C., Nogueira, I.C., de Oliveira, V.G., Lustosa, S.M.C., Longo, E., Cavalcante, L.S., 2015. Structural, morphological and optical investigation of β-Ag_2MoO_4 microcrystals obtained with different polar solvents. CrystEngComm 17, 8207–8211. https://doi.org/10.1039/C5CE01662B.
Donohue, J., Shand, W., 1947. The determination of the interatomic distances in silver molybdate. Ag_2MoO_4. J. Am. Chem. Soc. 69, 222–223. https://doi.org/10.1021/ja01194a010.
Driscoll, S.A., Gardner, D.K., Ozkan, U.S., 1994. Isotopic labeling studies on oxidative coupling of methane over alkali promoted molybdate catalysts. Catal. Lett. 25, 191–199. https://doi.org/10.1007/BF00816300.
Gan, G., Zhao, P., Zhang, X., Liu, Juan, Liu, Jingjing, Zhang, C., Hou, X., 2017. Degradation of Pantoprazole in aqueous solution using magnetic nanoscaled Fe_3O_4/CeO_2 composite: effect of system parameters and degradation pathway. J. Alloys Compd. 725, 472–483. https://doi.org/10.1016/j.jallcom.2017.07.063.
Gracia-Lor, E., Sancho, J.V., Serrano, R., Hernández, F., 2012. Occurrence and removal of pharmaceuticals in wastewater treatment plants at the Spanish Mediterranean area of Valencia. Chemosphere 87, 453–462. https://doi.org/10.1016/j.chemosphere.2011.12.025.
Hensley, K., Aksenova, M., Carney, J.M., Harris, M., Butterfield, D.A., 1995. Amyloid β-peptide spin trapping II: evidence for decomposition of the pbn spin adduct. Neuroreport. https://doi.org/10.1097/00001756-199502000-00022.
Hinojosa Guerra, M.M., Oller Alberola, I., Malato Rodriguez, S., Agüera López, A., Acevedo Merino, A., Egea-Corbacho Lopera, A., Quiroga Alonso, J.M., 2019. Oxidation mechanisms of amoxicillin and paracetamol in the photo-Fenton solar process. Water Res. 156, 232–240. https://doi.org/10.1016/j.watres.2019.02.055.
Hosseini, M., Kahkha, M.R.R., Fakhri, A., Tahami, S., Lariche, M.J., 2018. Degradation of macrolide antibiotics via sono or photo coupled with Fenton methods in the presence of ZnS quantum dots decorated SnO_2 nanosheets. J. Photochem. Photobiol. B Biol. 185, 24–31. https://doi.org/10.1016/j.jphotobiol.2018.05.022.
Huo, Y., Wang, Z., Zhang, J., Liang, C., Dai, K., 2018. Ag SPR-promoted 2D porous g-C_3N_4/Ag_2MoO_4 composites for enhanced photocatalytic performance towards methylene blue degradation. Appl. Surf. Sci. 459, 271–280. https://doi.org/10.1016/j.apsusc.2018.08.005.
Jiang, P., Li, S.Y., Xie, S.S., Gao, Y., Song, L., 2004. Machinable long PVP-stabilized silver nanowires. Chem. Eur J. 10, 4817–4821. https://doi.org/10.1002/chem.200400318.
Jungnickel, P.W., 2000. Pantoprazole: a new proton pump inhibitor. Clin. Therapeut. 22, 1268–1293. https://doi.org/10.1016/S0149-2918(00)83025-8.
Kosma, C.I., Lambropoulou, D.A., Albanis, T.A., 2016. Analysis, occurrence, fate and risks of proton pump inhibitors, their metabolites and transformation products in aquatic environment: a review. Sci. Total Environ. 569 (570), 732–750. https://doi.org/10.1016/j.scitotenv.2016.06.160.
Kumar, A., Sharma, S.K., Sharma, G., Al-Muhtaseb, A.H., Naushad, M., Ghfar, A.A., Stadler, F.J., 2019. Wide spectral degradation of Norfloxacin by Ag@$BiPO_4$/BiOBr/$BiFeO_3$ nano-assembly: elucidating the photocatalytic mechanism under different light sources. J. Hazard Mater. 364, 429–440. https://doi.org/10.1016/j.jhazmat.2018.10.060.
Ledwith, A., Russell, P.J., Sutcliffe, L.H., 1973. Alkoxy radical intermediates in the thermal and photochemical oxidation of alcohols. Proc. R. Soc. London. A. Math. Phys. Sci. 332, 151–166. https://doi.org/10.1098/rspa.1973.0018.
Li, J., Liu, F., Li, Y., 2018. Fabrication of an Ag/Ag_2MoO_4 plasmonic photocatalyst with enhanced photocatalytic performance for the degradation of ciprofloxacin. New J. Chem. 42, 12054–12061. https://doi.org/10.1039/c8nj02327a.
Lu, J., Qi, P., Peng, Y., Meng, Z., Yang, Z., Yu, W., Qian, Y., 2001. Metastable MnS crystallites through solvothermal synthesis. Chem. Mater. 13, 2169–2172. https://doi.org/10.1021/cm010049j.
Makal, P., Das, D., 2018. Self-doped TiO_2 nanowires in TiO_2-B single phase, TiO_2-B/anatase and TiO_2-anatase/rutile heterojunctions demonstrating individual superiority in photocatalytic activity under visible and UV light. Appl. Surf. Sci. 455, 1106–1115. https://doi.org/10.1016/j.apsusc.2018.06.055.
Márquez, J.J.R., Levchuk, I., Sillanpää, M., 2018. Application of catalytic wet peroxide oxidation for industrial and urban wastewater treatment: a review. Catalysts 8. https://doi.org/10.3390/catal8120673.
Moura, J.V.B., da Silva Filho, J.G., Freire, P.T.C., Luz-Lima, C., Pinheiro, G.S., Viana, B.C., Mendes Filho, J., Souza-Filho, A.G., Saraiva, G.D., 2016. Phonon properties of β-Ag_2MoO_4: Raman spectroscopy and ab initio calculations. Vib. Spectrosc. 86, 97–102. https://doi.org/10.1016/j.vibspec.2016.06.009.
Ng, C.H.B., Fan, W.Y., 2015. Uncovering metastable α-Ag_2MoO_4 phase under ambient conditions. overcoming high pressures by 2,3-Bis(2-pyridyl)pyrazine doping. Cryst. Growth Des. 15, 3032–3037. https://doi.org/10.1021/acs.cgd.5b00455.
Nogueira, R.F.P., Oliveira, M.C., Paterlini, W.C., 2005. Simple and fast spectrophotometric determination of H_2O_2 in photo-Fenton reactions using metavanadate. Talanta 66, 86–91. https://doi.org/10.1016/j.talanta.2004.10.001.
Oliveira, C.A., Volanti, D.P., Nogueira, A.E., Zamperini, C.A., Vergani, C.E., Longo, E., 2017. Well-designed β-Ag_2MoO_4 crystals with photocatalytic and antibacterial activity. Mater. Des. 115, 73–81. https://doi.org/10.1016/j.matdes.2016.11.032.
Ortiz de García, S., Pinto Pinto, G., García Encina, P., Irusta Mata, R., 2013. Consumption and occurrence of pharmaceutical and personal care products in the aquatic environment in Spain. Sci. Total Environ. 444, 451–465. https://doi.org/10.1016/j.scitotenv.2012.11.057.
Penghui, S., Duan, X., Xu, J., Tian, J., Shi, W., Gao, S., Xu, M., Cui, F., Wang, S., 2017. Heterogeneous activation of peroxymonosulfate by amorphous boron for degradation of bisphenol S. J. Hazard Mater. 322, 532–539. https://doi.org/10.1016/j.jhazmat.2016.10.020.
Raffin, R.P., Colomé, L.M., Schapoval, E.E.S., Pohlmann, A.R., Guterres, S.S., 2008. Increasing sodium pantoprazole photostability by microencapsulation: effect of the polymer and the preparation technique. Eur. J. Pharm. Biopharm. 69, 1014–1018. https://doi.org/10.1016/j.ejpb.2008.01.024.
Raha, S., Ahmaruzzaman, M., 2020. Facile fabrication of g-C_3N_4 supported Fe_3O_4 nanoparticles/ZnO nanorods: a superlative visible light responsive architecture for express degradation of pantoprazole. Chem. Eng. J. 387, 123766. https://doi.org/10.1016/j.cej.2019.123766.
Rosen, G.M., Britigan, B.E., Halpern, H.J., Pou, S., 1999. Free Radicals: Biology and Detection by Spin Trapping. Oxford University Press on Demand.
Saha, B., Kumar, S., Sengupta, S., 2019. Green synthesis of nano silver on TiO_2 catalyst for application in oxidation of thiophene. Chem. Eng. Sci. 199, 332–341. https://doi.org/10.1016/j.ces.2018.12.063.
Saprin, A.N., Piette, L.H., 1977. Spin trapping and its application in the study of lipid peroxidation and free radical production with liver microsomes. Arch. Biochem. Biophys. 180, 480–492. https://doi.org/10.1016/0003-9861(77)90063-7.
Sharma, G., Dionysiou, D.D., Sharma, S., Kumar, A., Al-Muhtaseb, A.H., Naushad, M., Stadler, F.J., 2019. Highly efficient Sr/Ce/activated carbon bimetallic nanocomposite for photoinduced degradation of rhodamine B. Catal. Today 335, 437–451. https://doi.org/10.1016/j.cattod.2019.03.063.
Sousa, G. da S., Nobre, F.X., Araújo Júnior, E.A., Sambrano, J.R., Albuquerque, A. dos R., Bindá, R. dos S., Couceiro, P.R. da C., Brito, W.R., Cavalcante, L.S., Santos, M., de Matos, J.M.E., 2018. Hydrothermal synthesis, structural characterization and photocatalytic properties of β-Ag_2MoO_4 microcrystals: correlation between experimental and theoretical data. Arab. J. Chem. https://doi.org/10.1016/j.arabjc.2018.07.011.
Standard, I., 2007. International Standard of the Inhibitory Effect of Water Samples 2007.
Stoll, S., Schweiger, A., 2006. EasySpin, a comprehensive software package for spectral simulation and analysis in EPR. J. Magn. Reson. 178, 42–55. https://doi.org/10.1016/j.jmr.2005.08.013.
Teranishi, T., Miyake, M., 1998. Size control of palladium nanoparticles and their crystal structures. Chem. Mater. 10, 594–600. https://doi.org/10.1021/cm9705808.
Thommes, M., Kaneko, K., Neimark, A.V., Olivier, J.P., Rodriguez-Reinoso, F., Rouquerol, J., Sing, K.S.W., 2015. Physisorption of gases, with special reference to the evaluation of surface area and pore size distribution (IUPAC Technical Report). Pure Appl. Chem. 87, 1051–1069. https://doi.org/10.1515/pac-2014-1117.
Valeeva, A.A., Kozlova, E.A., Vokhmintsev, A.S., Kamalov, R.V., Dorosheva, I.B., Saraev, A.A., Weinstein, I.A., Rempel, A.A., 2018. Nonstoichiometric titanium dioxide nanotubes with enhanced catalytical activity under visible light. Sci. Rep. 8, 1–10. https://doi.org/10.1038/s41598-018-28045-1.
Vieira, G.B., José, H.J., Peterson, M., Baldissarelli, V.Z., Alvarez, P., de Fátima Peralta Muniz Moreira, R., 2018. CeO_2/TiO_2 nanostructures enhance adsorption and photocatalytic degradation of organic compounds in aqueous suspension. J. Photochem. Photobiol. Chem. 353, 325–336. https://doi.org/10.1016/j.jphotochem.2017.11.045.
Wang, Q., Qiao, Z., Jiang, P., Kuang, J., Liu, W., Cao, W., 2018. Hydrothermal synthesis and enhanced photocatalytic activity of mixed-phase TiO_2 powders with controllable anatase/rutile ratio. Solid State Sci. 77, 14–19. https://doi.org/10.1016/j.solidstatesciences.2018.01.003.
Wang, Z., Dai, K., Liang, C., Zhang, J., Zhu, G., 2017. Facile synthesis of novel butterfly-like Ag_2MoO_4 nanosheets for visible-light driven photocatalysis. Mater. Lett. 196, 373–376. https://doi.org/10.1016/j.matlet.2017.03.078.
Wyckoff, R.W.G., 1922. The crystal structure of silver molybdate. J. Am. Chem. Soc. 44, 1994–1998. https://doi.org/10.1021/ja01430a017.
Xu, D., Cheng, B., Zhang, J., Wang, W., Yu, J., Ho, W., 2015. Photocatalytic activity of Ag_2MO_4 (M = Cr, Mo, W) photocatalysts. J. Mater. Chem. 3, 20153–20166. https://doi.org/10.1039/c5ta05248c.
Yang, X., Wang, Y., Xu, X., Qu, Y., Ding, X., Chen, H., 2017. Surface plasmon resonance-induced visible-light photocatalytic performance of silver/silver molybdate composites. Cuihua Xuebao/Chinese J. Catal. 38, 260–269. https://doi.org/10.1016/S1872-2067(16)62553-6.
Zhao, H., Joseph, J., Zhang, H., Karoui, H., Kalyanaraman, B., 2001. Synthesis and biochemical applications of a solid cyclic nitrone spin trap: a relatively superior trap for detecting superoxide anions and glutathiyl radicals. Free Radic. Biol. Med. 31, 599–606. https://doi.org/10.1016/S0891-5849(01)00619-0.